JREE: Vol. 12, No. 2, (Spring 2025) 115-128

Journal of Renewable Energy and Environment

Journal Homepage: www.jree.ir

Materials and Energy Research Center

MERC

Research Article

Robust Controllers for Precision Power Sharing among DG Units of Islanded Microgrid Under Load Variations

Oinam Manganleiba Meetei[a], Marimuthu Prakash[b]*, Rajagopal Kumar[b]

[a] Department of Electrical Engineering, Manipur Technical University, Imphal, Manipur, P.O. Box: 795004, India.
[b] Department of Electrical and Electronics Engineering, National Institute of Technology, Nagaland, P.O. Box: 797103, India.

PAPER INFO

Paper history:
Received: 21 November 2024
Revised: 07 March 2025
Accepted: 11 May 2025

Keywords:
Droop Control,
Proportional Integral Control,
Higher Order Sliding Mode Control (HOSMC),
Single Hidden Layer Feed-Forward Neural Network (SHLFFNN),
Distributed Generation (DG),
Battery pack

ABSTRACT

Islanded microgrids are prone to frequent fluctuations in power sharing among distributed generation (DG) units. This is primarily due to the microgrids inherent characteristics, such as load uncertainty, the lack of accurate control methods, and the variable generation patterns of renewable energy sources. The droop control method combined with a Proportional-Integral (PI) anti-windup technique alone is insufficient for ensuring proper power sharing among DG units. It also struggles to maintain standard voltage and frequency levels. This research proposes a droop control approach based on real power and frequency, combined with higher-order sliding mode control and a single hidden layer feed-forward neural network. The higher-order sliding mode controller is responsible for regulating the voltage, while the single hidden layer feed-forward neural network is employed to control the current. The controllers are designed to ensure equal power sharing among DG units even as the load varies. Experiments are conducted under three different loading conditions to evaluate the stability of power sharing among the DG units. To verify the effectiveness of the proposed method, the real and reactive power sharing between DG1 and DG2 is compared using both the existing and proposed controllers across each case. Additionally, to assess the robustness of the controller, voltage and frequency comparisons are carried out under time-varying load conditions against other controllers. The proposed microgrid is modeled and simulated in the MATLAB/Simulink environment. The simulation results demonstrate that the proposed controllers significantly enhance the performance of the droop controller and achieve equal power sharing among DG units despite load variations.

https://doi.org/10.30501/jree.2025.487895.2159

1. INTRODUCTION

Non-renewable energy sources such as coal, oil, and other materials contribute to more than 70 percent of global warming. However, positive steps have been taken to shift energy production from conventional sources to more efficient and environmentally friendly alternatives. Advances in research have led to the development of various alternative energy sources. Different methods of electricity distribution systems have been developed based on these renewable energy sources, with microgrids being a prominent example. The need for microgrids has increased due to their advantages in off-grid site electrification, reduced burden on centralized grids, and improved utilization of renewable energy sources. Consequently, microgrids are expanding rapidly across different regions. Over the past few decades, advancements in power electronic converters have enabled microgrids to integrate power sources such as solar energy, fuel cells, and hydropower as distributed generation (DG) units.

In a grid-connected microgrid system, the voltage and frequency of the DG units are determined by the main grid. However, in an isolated microgrid system, the DG units' voltage and frequency are independent of the main grid. Variations in power generation and load frequently disrupt power sharing, voltage, and frequency stability in isolated microgrid systems. This leads to increased uncertainties within the microgrid (Geravandi & Moradi CheshmehBeigi, 2022; Hassan Moradi CheshmehBeigi, 2023). The active and reactive power demanded by the load is supplied by the DGs through DC-AC converters. Stable active and reactive power sharing among DGs is essential to maintain reliable voltage and frequency levels in microgrids. Therefore, a reliable control mechanism is necessary to ensure steady operation. Several control mechanisms have been implemented for microgrid management. Among them, droop control is a significant method for power sharing among DGs. In this technique, voltage and frequency (v–f) are adjusted based on real power and reactive power (P–Q) characteristics. Regulation of frequency for multiple microgrids operating in parallel is achieved through the voltage droop control scheme (Jalilian et al., 2023). These control techniques also encounter issues in terms of accuracy, speed, and robustness (Tran et al., 2018). Traditional droop control supports only small-signal stability (Ma et al., 2012), and even then, it often fails to achieve proper power sharing between DGs due to inequalities in the feeder impedance of voltage source inverters (Keyvani et al., 2022). Moreover, feeder impedance varies as the load changes. Several strategies for enhancing droop control have been proposed in various academic studies. Frequency and angle

*Corresponding Author's Email: mangal.oinam@gmail.com (O. M. Meetei)
URL: https://www.jree.ir/article_220633.html

Please cite this article as: Meetei, O. M., Prakash, M. & Kumar, R. (2025). Robust Controllers for Precision Power Sharing among DG Units of Islanded Microgrid Under Load Variations, *Journal of Renewable Energy and Environment (JREE)*, 12(2), 115-128. https://doi.org/10.30501/jree.2025.487895.2159

droop control methods have been suggested for distributing total load among generating units operating in autonomous mode. Improved droop control techniques and adaptive decentralized droop control strategies have been proposed to achieve equal power sharing among parallel-connected inverters (Hoa Thi Pham, 2020; Poonahela et al., 2023). Maintaining reactive power sharing among DGs can correct voltage and frequency discrepancies (Micallef et al., 2014; Shayeghi & Rahnama, 2024). In a low-voltage microgrid, voltage and frequency can be controlled by defining the relationships between active power and voltage (P–V), and reactive power and frequency (Q–f) (Abjadi, 2024). In a multi-converter autonomous system, to achieve a uniform frequency across all converters, the direct and quadrature (*dq*)-axis frequency of the first converter is used as a reference for all other units. The stability of microgrid operation depends on the eigenvalues and parameters within the controller domain. The role of the controllers is to ensure that parameter variations remain within allowable bounds (Guerrero et al., 2011). Correcting voltage and frequency mismatches and achieving power-sharing in minimum time are essential objectives for ensuring a reliable microgrid. A distributed secondary control approach, utilizing a minimum variance control method combined with a finite-time consensus algorithm, has been proposed to address these challenges (Habibi et al., 2024; Wu et al., 2024). Proportional–Integral (PI) controllers have also been employed to manage microgrid voltage and power (Hossain & Pota, 2015). However, PI controllers exhibit poor voltage regulation capability and are less resilient against certain voltage uncertainties (Sarkar & Das, 2018; Sofla & Gharehpetian, 2011). Several algorithms have been developed to tune the parameters of Proportional–Integral–Derivative (PID) controllers, including the Genetic Algorithm (GA) (Das et al., 2012), Particle Swam Optimization (PSO) (Pandey et al., 2014), and Social Spider Optimizer (SSO) (El-Fergany & El-Hameed, 2017), etc. A derivative filter-based PID controller has been proposed to mitigate voltage and frequency imbalances in microgrids. Moreover, objective functions for tuning PID parameters have been established using the Jaya algorithm (Mamta et al., 2024; Amarendra et al., 2023). Recent advancements in artificial intelligence (AI) have also been reviewed for improving microgrid stability (Ko et al., 2020; Rangu et al., 2020). The Modified Shuffled Frog Leaping Algorithm (MSFLA) has been used to enhance electricity quality and reliability in distribution networks (Moazzami et al., 2017). Additionally, Swarm Intelligence (SI)-based optimized controllers have been implemented to address voltage, frequency, and power-sharing challenges in microgrids (Jumani et al., 2020; Al-Saedi et al., 2012). However, most of the algorithms proposed for microgrid control exhibit slow execution speeds, while microgrids demand faster responses to counter dynamic deviations. The Single Hidden Layer Feedforward Neural Network (SHLFFNN) has the advantage of fast execution, making it more efficient for controlling the current of DGs. Since SHLFFNN focuses solely on current control, it requires less computation time and delivers efficient performance. Sliding Mode Control (SMC) is another nonlinear control approach known for its high reliability. It can guide the system's behavior onto a pre-designed sliding surface (Šabanovic, 2011).

Traditional SMC methods have been proposed for controlling single-phase microgrids by employing linear sliding surfaces (Abrishamifar et al., 2012). However, conventional SMC suffers from the chattering phenomenon, which can shorten equipment life span and cause errors that prevent convergence within a bounded time. It can also distort output voltages under nonlinear loads. Higher-order sliding mode controllers (HOSMC) offer improved accuracy in power-sharing across varying load conditions. By eliminating discontinuous terms and increasing the relative degree, HOSMC can mitigate chattering effects. Researchers have explored using HOSMC for controlling islanded microgrids. For instance, a second-order sliding control system was designed for a voltage source inverter (VSI) (Cucuzzella et al., 2015). However, the VSI output voltage remained discontinuous and unstable. In (Cucuzzella et al., 2015b) the same study, a third-order SMC was designed using a combination of linear sliding surfaces, achieving only asymptotic stability. In islanded microgrid models, the third-order SMC design (Cucuzzella et al., 2015a) can yield continuous control action by increasing the relative degree, which may improve the transient response.

After reviewing the studies conducted on power-sharing among microgrids, and on voltage and frequency magnitude stability, it has been observed that there is still no highly effective controller capable of accurately sharing power and regulating voltage and frequency variations. Several limitations have been identified for further research:

- The existing droop control method is unable to manage impedance mismatches effectively.
- Damping oscillations cannot be stabilized within a short period under high-load conditions.
- Using only droop control combined with PI and SMC controllers fails to adequately share real and reactive power demand among DGs, and does not sufficiently ensure voltage and frequency magnitude stability.

To address these challenges, new control strategies are proposed to enhance the performance of droop control. A combined control approach is suggested, integrating droop control with Higher-Order Sliding Mode Control (HOSMC) and Single Hidden Layer Feed-Forward Neural Network (SHLFFNN) artificial intelligence algorithms. This combined strategy aims to regulate voltage and frequency while achieving equal sharing of real and reactive power among DGs. The control laws are specifically designed and trained to reject disturbances. HOSMC, which belongs to the same family as SMC, utilizes a nonlinear sliding surface. It provides finite-time convergence and exhibits high robustness under heavy loads and uncertain operating conditions. By combining these controllers, it is expected to achieve smoother output voltage and frequency responses, thereby improving system stability.

The primary contributions of this work are summarized as follows:

- Implementation of an improved droop control technique based on real power and frequency dynamics.
- Design of a nonlinear sliding surface tailored to the proposed system's conditions.
- Introduction of a novel control approach combining Higher-Order Sliding Mode Control with a Single Hidden Layer Feed-Forward Neural Network.

- Consideration of three uncertainty conditions to ensure robust controller performance.

The structure of the paper is as follows: Sections 2 and 3 present the configuration and design of the proposed islanded microgrid. Section 4 addresses the modeling of the battery pack. Section 5 discusses the design of the proposed control methods. In Section 6, simulation results are provided, and the performance of the proposed controller is compared with various other control strategies. Finally, Section 7 concludes the study.

2. ISLANDED MICROGRID SYSTEM

Figure 1 illustrates the proposed schematic of an islanded microgrid system. The microgrid consists of two comparable.

DG units, comparable DG units, each connected to its own load, and interconnected via a transmission line. The design specifications used in the schematic are provided in Table 1. Additionally, three inverters rated at 500 kW, 300 kW, and 200 kW are connected in parallel, with their ratings detailed in Table 2. All converters utilize batteries as their primary energy source. Step-down transformers are connected to each converter, enabling them to collectively supply a common load. The proposed islanded microgrid system is designed to operate under three different load patterns. To reduce converter output noise and minimize voltage fluctuations at the load connection points, capacitors are installed, resulting in a more stable load voltage. The four main components of the control sequence, as shown in Figure 2, are:

a) Droop control to distribute power equally among the DG units;

b) Voltage regulation to maintain nearly constant voltage despite load variations;

c) Current regulation to stabilize the output current against fluctuations;

d) Reference frame transformations (*dq* to *Vabc* and vice versa) combined with a pulse-width modulation (PWM) signal generation block. Voltage control is performed using the proposed adaptive Higher-Order Sliding Mode Control (HOSMC) with carefully tuned gain settings. Meanwhile, current control is managed by the trained Single Hidden Layer Feed-Forward Neural Network (SHLFFNN). Together, these methods enhance the performance of the frequency-based droop control and improve the accuracy of power-sharing among DG units. The SHLFFNN is trained using the Levenberg–Marquardt algorithm. Training data is generated under various loading conditions, including linear resistive-inductive (RL) loads, constant loads, and variable nonlinear loads, allowing the network to adapt to a wide range of operating environments. After training, the feed-forward neural network (FFNN) is implemented individually within each DG unit of the microgrid system.

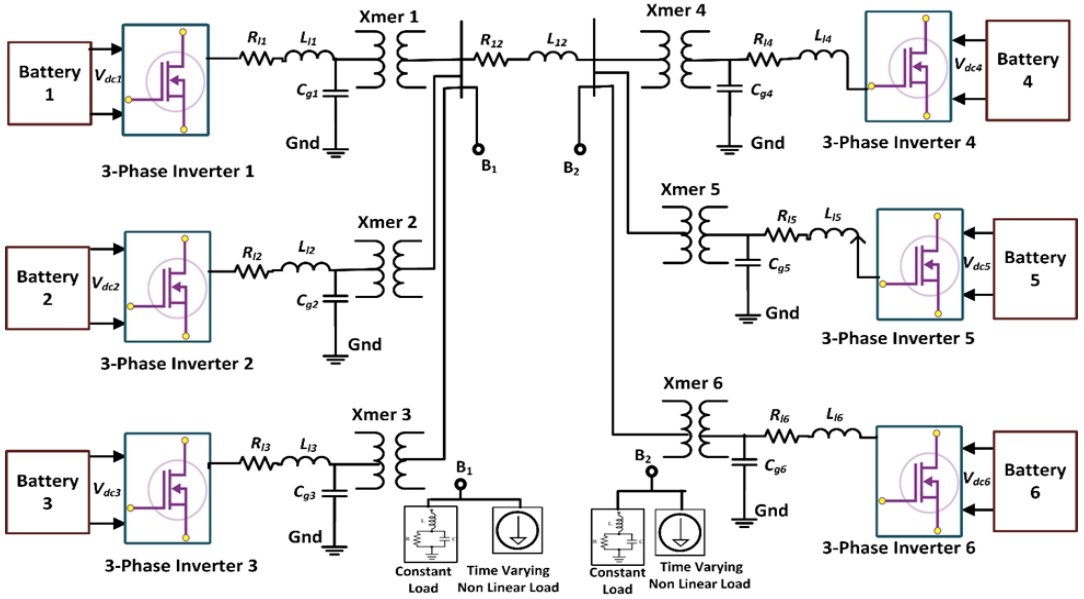

Figure 1. The study system's schematic diagram.

Table 1. Values of system parameters selected for the proposed microgrid.

System Parameters	Values
Nominal AC voltage	440V (L-G)
Frequency	50Hz
Nominal battery voltage (V_{dci})	800V
Battery capacity	100Ah
Initial state of charge (%)	100
Transformer Winding 1 & 2 parameters	
Winding resistance, R(pu)	0.0015
Winding inductance, L(pu)	0.03
Magnetization resistance, R_m(pu)	200
Magnetization inductance, L_m(pu)	200
Nominal ratings, s	450kVA
Voltage Ratio	480/440

Transmission Line Parameters	
Positive Resistance	0.01273 Ω/km
Zero Sequence Resistance	0.3864 Ω/km
Positive Inductance	0.9337 mH/km
Zero Sequence Inductance	4.1264 mH /km
Positive Capacitance	12.74x 10-9 F/km
Zero Sequence Capacitance	7.751x10-9mH /km

Table 2. Parameters used in DG1 & DG2 Inverters.

Inverter 1	Inverter 2	Inverter 3
Rated power=500kW	Rated power=300kW	Rated power=200kW
LC filter	LC filter	LC filter
R_f=0.15Ω, L_f=0.15H, C_f=0.05uf	R_f=0.15Ω, L_f=0.15H, C_f=0.05uf	R_f=0.15Ω, L_f=0.15H, C_f=0.05uf
Controller		
PI Voltage Regulation K_p=2, k_i=14	PI Voltage Regulation K_p=2, k_i=10	PI Voltage Regulation K_p=2, k_i=12
PI Current Regulation K_p=0.3, k_i=20	PI Current Regulation K_p=0.3, k_i=20	PI Current Regulation K_p=0.3, k_i=20
Voltage droop(%)=4 Frequency droop(%)=1	Voltage droop(%)=4 Frequency droop(%)=1	Voltage droop(%)=4 Frequency droop(%)=1
Sliding Surfaces g_1=0.02, g_2 = 0.04	Sliding Surfaces g_1=0.02, g_2 = 0.04	Sliding Surfaces g_1=0.02, g_2 = 0.04
SMC Voltage Regulation K=13, α=6, c=0.0004	SMC Voltage Regulation K=13, α=6, c=0.0004	SMC Voltage Regulation K=13, α=6, c=0.0004

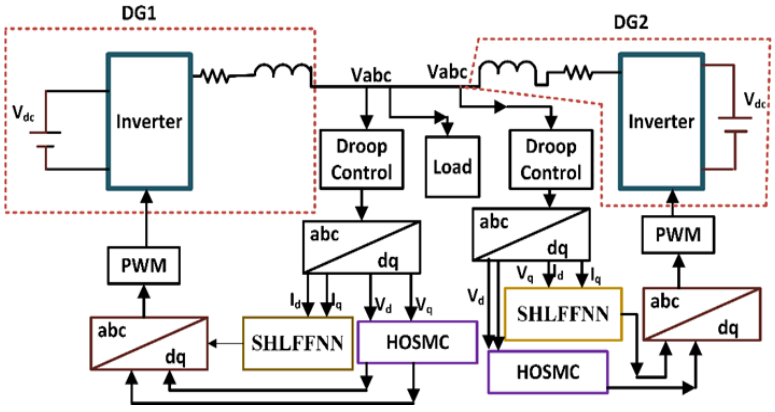

Figure 2. The proposed control sequence schematic diagram.

3. SYSTEM DYNAMIC EQUATIONS AND MODELING

To increase the load handling capacity, inverters are connected in parallel. The system dynamic equation is translated into the d-q-axis reference frame. The equations are given below ($i = 1,2$):

$$V_{oid} = V_{lid} - R_{li}I_{pid} - L_{li}\frac{d}{dt}I_{pid} + \omega_{li}L_{li}I_{pid} = M_{id}\frac{V_{dci}}{2} \quad (1)$$

$$V_{oiq} = V_{liq} - R_{li}I_{piq} - L_{li}\frac{d}{dt}I_{piq} - \omega_{li}L_{li}I_{piq} = M_{iq}\frac{V_{dci}}{2} \quad (2)$$

where V_{oid} & V_{oiq} are the output phase voltages of d & q reference frames, V_{lid} & V_{liq} are the load voltages of the direct & quadrature axes, L_{li}, R_{li} are the transmission line inductance & resistance, I_{pid} & I_{piq} are the phase current of d & q axis, M_i is the modulation index, ω_{li} is the frequency.

The capacitor voltage equation is given as:

$$C_{gi}\frac{d}{dt}V_{oid} = I_{pid} - I_{ijd} - I_{nid} - I_{id} - I_{ibnd} - I_{xifl} + \omega_{li}C_{gi} \quad (3)$$

$$C_{gi}\frac{d}{dt}V_{oiq} = I_{piq} - I_{ijq} - I_{niq} - I_{iq} - I_{ibnq} - I_{xifl} - \omega_{li}C_{gi}V_{oid} \quad (4)$$

where C_{gi}, I_{xifl} are the capacitance of distributed generation and filter current, respectively, and I_{pi}, I_{ij}, I_{ni}, I_{ibn}, I_i, V_{oi} are the phase currents, currents between two converters, linear load currents, non-linear load currents, phase current of constant load, and load voltage components of d & q axes, respectively. The equations for the transmission line between converters are given below:

$$V_{oid} - V_{oiq} = R_{12}I_{ijd} + L_{12}\frac{d}{dt}I_{ijd} - \omega_{li}L_{12}I_{ijq} \quad (5)$$

$$V_{oiq} - V_{oiq} = R_{12}I_{ijd} + L_{12}\frac{d}{dt}I_{ijq} + \omega_{li}L_{12} \quad (6)$$

where L_1 & R_{12} are the inductance and resistance of the connecting line.

4. MODELING OF BATTERY PACK

The smallest unit of a battery system is the cell. A single battery cell typically has limited capacity and insufficient voltage to supply a microgrid. To meet the total capacity and voltage requirements of the microgrid, a battery pack must be assembled using multiple cells. In a series connection, cells are linked from the positive terminal of one cell to the negative terminal of the next, increasing the overall voltage. In a parallel connection, cells are connected positive to positive and negative to negative, which extends the runtime while maintaining a constant voltage. Battery modules are groups of cells arranged in series and/or parallel configurations. To achieve the desired overall voltage for the microgrid, multiple battery modules are further connected in series and/or parallel.

The battery model incorporates Open Circuit Voltage (OCV) into the equation of State of Charge (SOC). Polarization voltage is added while the polarization resistance is only minimally altered. The battery voltage equation (Damiano et al., 2015) is given as:

$$V_{batt} = E_o - K\frac{Q}{Q-it}\,it - Ri + Aexp(-B.it) - K\frac{Q}{Q-it}\,i^* \quad (7)$$

where $V_{batt}, E_o, K, Q, A, B, R, i^*, i$ are the battery terminal voltage *(V)*, battery steady voltage *(V)*, polarization constant *(V/Ah)*, battery capacity *(Ah)*, exponential zone amplitude*(V)*, exponential zone time constant inverse $(Ah)^{-1}$, internal resistance *(Ω)*, and filtered current *(A)*, respectively, and $it = \int idt$ = true battery charge *(Ah)*.

The charging and discharging of a battery determines how long it will last. The corresponding equations (Damiano et al., 2015) are defined as:

$$V_{batt} = E_o - Ri - K\frac{Q}{Q-it}\,it + Aexp(-B.it) - K\frac{Q}{it-0.1Q}\,i^* \quad (8)$$

Discharging:

$$V_{batt} = E_o - Ri - K\frac{Q}{Q-it}\,(it + i^*) + Aexp(-B.it) \quad (9)$$

As a result, specific parameters are defined, with the lower and upper limits of the state of charge (SOC) set at 20% and 80%, respectively (Mishra, 2013). The SOC is typically determined by calculating the ratio of the battery's remaining capacity to its total capacity. Theoretically, it can be estimated using the ampere-hour integration method, which involves integrating the measured battery current over time (Mawuntu et al., 2023) as:

$$SOC(t) = SOC(t_o) - \int_{t_o}^{t}\frac{I_L(t)\eta}{C_r}\,dt \quad (10)$$

where *SOC(t)* and $SOC(t_0)$ are the present and initial states of charge, respectively, C_r is the maximum available capacity, η is the cell's Coulombic efficiency, and $I_L(t)$ is the load current. Eq. (11) is used to obtain the battery's Ah rating.

$$Ah_{req} = \frac{Watt_{req}*hr}{V_{batt}*DoD} \quad (11)$$

where Ah_{req}=required hour, $Watt_{req}$=required wattage, *hr*=No. of hours, V_{batt}=battery voltage, and *DoD* = depth of discharge. In this case, it is assumed that no current is supplied from renewable sources. The battery is expected to support the load even with a 40% depth of discharge. Based on this condition, a battery capacity of 100 Ah is selected for simulation.

5. DESIGN OF CONTROLLERS

5.1 Droop control

Droop control uses reactive power and active power as function parameters to control frequency and output power magnitude (Vigneysh & Kumarappan, 2016). The relationships among them are given as:

$$\omega_i^* = \omega_n - m_i P_{oi} \quad (12)$$

$$V_i^* = V_n - n_i Q_{oi} \quad (13)$$

where V_n and ω_n are the rated voltage and frequency. *m*, *n*, P_o, Q_o are real power develop coefficients, reactive power droop coefficients, output active power, and output reactive power, respectively. From Eqs. (12) and (13), the droop coefficients are written into:

$$m_i = \frac{\Delta\omega}{\Delta P_{oi}} \quad (14)$$

$$n_i = \frac{\Delta V_o}{\Delta Q_{oi}} \quad (15)$$

To keep the entire system's frequency constant, the parameters of two DGs are equated as:

$$\omega_n - m_1 P_{01} = \omega_n - m_2 P_{02} \quad (16)$$

$$\omega_n - m_2 P_{02} = \omega_n - m_3 P_{03} \quad (17)$$

$$\frac{m_1}{m_2} = \frac{P_{o2}}{P_{o1}}, \frac{m_2}{m_3} = \frac{P_{o3}}{P_{o2}} \quad (18)$$

The computed instantaneous output active and reactive powers is:

$$P_o^* = \frac{3}{2}(V_{oq}I_{pq} + V_{od}I_{pq}) \quad (19)$$

$$Q_o^* = \frac{3}{2}(V_{oq}I_{pq} + V_{od}I_{pq}) \quad (20)$$

The filter's low-pass fundamental components, which are provided as follows, are utilized to calculate the real and reactive powers.

$$P_o = \frac{\omega_c}{s+\omega_c}P_o^* \quad (21)$$

$$Q_o = \frac{\omega_c}{s+\omega_c}Q_o^* \quad (22)$$

where ω_c=cut of frequency. The reference voltage for the *dq*-axis is determined as:

$$V_{oq} = V_o\cos(\theta_i^* - \theta) \quad (23)$$

$$V_{od} = -V_o\sin(\theta_i - \theta) \quad (24)$$

where V_o is the load voltage of *dq* transformation and the reference angle is represented as θ.

5.2 HOSMC-Based Voltage Control

Figure 3 illustrates the control diagram of the higher-order sliding mode. After converting V_{abc} into the *dq* reference frame, the resulting *d* and *q* signals are compared to their predefined reference values using the formulas provided in Equations (25)–(28).

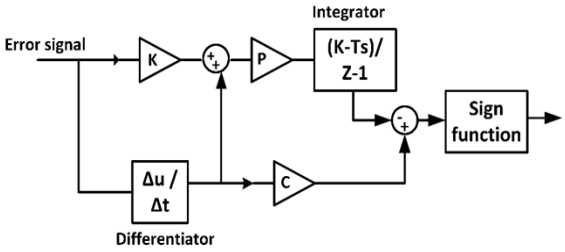

Figure 3. HOSMC Control unit diagram.

To allow for a more detailed analysis of the errors, the error signals are differentiated. A sliding surface is then defined through Equations (29) and (30) to maintain the system's performance within the desired trajectory. The control laws, introduced in Equations (31) and (32), are designed to ensure that the system tracks the sliding surface accurately, relying on the appropriate selection of gain values. While the hit-and-trial method is used to determine these gains, identifying suitable values remains a challenging task. The parameters associated with the control design are listed in Table 2. Selecting values close to those of the practical system helps in achieving stable sliding motion. Verification of the control law's existence on the sliding surface and its stability is addressed in Remark 1 and Theorem 1, respectively. The *d*-axis voltage error and its derivative are defined below:

$$x_1 = V_{od} - V_{od}^* \quad (25)$$

$$x_2 = \dot{x_1} = \frac{d}{dt}(V_{od} - V_{od}^*) \quad (26)$$

where V_{od}^* is the reference to V_{od} axis. The q-axis voltage error and its derivative are defined below:

$$x_3 = V_{oq} - V_{oq}^* \quad (27)$$

$$x_4 = \dot{x_3} = \frac{d}{dt}(V_{oq} - V_{oq}^*) \quad (28)$$

where V_{oq}^* is the reference to V_{oq} axis. The nonlinear sliding surfaces of dq- axis are defined as follows:

$$S_d = g_1 x_3 + x_4 \quad (29)$$

$$S_q = g_2 x_1 + x_2 \quad (30)$$

where g_1, g_2 are + ve odd integers .The axis input control signals d and q can be defined as:

$$u_d = kx_1 + \frac{d}{dt}x_1 + c\dot{x_1} - p\int \text{sign}(S_d)\, dt \quad (31)$$

$$u_q = kx_3 + \frac{d}{dt}x_3 + c\dot{x_3} - p\int \text{sign}(S_q) dt \quad (32)$$

where k , c, and p are the +ve gains.

Remark 1 (Makarenkov, 2017**)** The existence of a sliding mode requires a sufficient condition given as:

$$\frac{1}{2}\frac{d}{dt}S^2 < -\sigma|S| \quad (33)$$

where σ is +ve constant. The sign(◦) function is characterized as:

$$\text{Sign(s)} = \left.\begin{matrix} 1 \text{ for } s > 0 \\ 0 \text{ for } s = 0 \\ -1 \text{ for } s < 0 \end{matrix}\right\} \quad (34)$$

The state trajectories converge to the sliding surface (s=0), maintaining the trajectory within the boundaries of the origin. The following conditions must be met to ensure that the state trajectory remains at $s = 0$.

$$\left.\begin{matrix} S_d\dot{S_d} < 0 \\ S_q\dot{S_q} < 0 \end{matrix}\right\} \quad (35)$$

Theorem 1. Let the sliding surface equation be Eq. (29). The preferred controller law is created for the system defined in Eqs. (1) to (6) using Eqs. (31) and (32), and after a specific period, the tracking errors will disappear. Proof:- The dq-axis equations using the Lyapunov function are given as:
For d- axis

$$V = \frac{1}{2}s_d^2 \quad (36)$$

From Eqs. (29) and (31), the following equation can be rewritten:

$$\dot{s_d} = \frac{d}{dt}(V_{od} - V_{od}^*) - \propto \int \text{sign}(S_d) dt \quad (37)$$

where $\propto$ is the sliding gain. Taking the derivative of Eq. (36) and using Eq. (37), we have:

$$\dot{V} = s_d\dot{s_d} = s_d\frac{d}{dt}(V_{od} - V_{od}^*) - \propto \int \text{sign}(S_d)s_d dt \quad (38)$$

Considering $sign(S_d)s_d = \eta|s_d|$, where $0 < \eta < 1$, we can have:

$$s_d\dot{s_d} \leq -\eta|s_d| \quad (39)$$

For q- axis

$$V = \frac{1}{2}s_q^2 \quad (40)$$

From Eqs. (30) and (32), the following equation can be rewritten:

$$\dot{s_q} = \frac{d}{dt}(V_{oq} - V_{oq}^*) - \propto \int \text{sign}(S_q)\, dt \quad (41)$$

Taking the derivative of Eq. (40) and using Eq. (41), we have:

$$\dot{V} = s_q\dot{s_q} = s_q\frac{d}{dt}(V_{oq} - V_{oq}^*) - \propto \quad (42)$$

Considering $sign(S_q)s_q = \eta|s_q|$, where $0 < \eta < 1$, we have:

$$s_q\dot{s_q} \leq -\eta|s_q| \quad (43)$$

Thus, Equations (39) and (43) demonstrate that the variables satisfy the Lyapunov stability condition. Consequently, it can be concluded that the HOSMC will converge to the equilibrium point within a specified time. The tracking error in the HOSMC will be eliminated within this time frame, ensuring the stability of the DGs.

5.3 SHLFFNN-Based Current Control

Numerous applications use intelligent control techniques like fuzzy logic, ANN, and others (Hassan & Abido, 2011; Anbazhagan & Kumarappan, 2011). Among other techniques that exist to control the microgrid, the ANN-based controlling technique is essential for use (Hong & Chen, 2014; Gamez Urias et al., 2015). The performance of the neural network is influenced by factors such as the number of neurons, the activation function, and the training method used. The network consists of an input layer with two perceptron's, a hidden layer with ten perceptron's, and an output layer with one perceptron. Current regulation is achieved using a SHLFFNN controller, with the structure of the SHLFFNN shown in Figure 4.

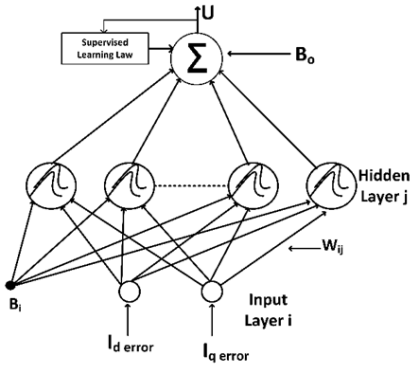

Figure 4. Structure of SHLFFNN.

The design algorithm for the SHLFFNN is described in detail below:

5.3.1 SHLFFNN nodes operation

Layer 1: Input Layer

These neuron layers are used to receive the input data and forward it to the hidden layer. The updates for the input and output layers are as follows:

$$P_i^1 = X_i^1(N) \quad (44)$$

$$Y_i^1(N) = f_i^1 P_i^1(N) = P_i^1(N) \quad i = 1,2. \quad (45)$$

where N represents the N^{th} iteration; $X_i^1(N)$ is the switching surface.

Layer 2: Hidden Layer

The number of neurons in the hidden layer, the activation function, and the training technique are all directly linked to the output performance of the SHLFFNN.
The expression for the hidden layer is:

$$H_i = \sigma(W_{ij}^{IH} * X_i + B_i^H) \quad (46)$$

where W_{ij}^{IH} is the updated weight; B_i^H is the bias of the hidden layer:

$$\sigma = \frac{1}{1+\exp^{-2X_i}} \quad i, j=1,2,3,..... \quad (47)$$

The activation function is defined as follows:

$$\emptyset_h = \frac{2}{1+\exp^{(-2*(W_{ij}^{IH}*X_i+B_i^H))}} - 1 \quad \text{for ij} = 1,2,3 \ldots \quad (48)$$

The Levenberg-Marquardt algorithm uses the gradient descent method to determine the weight change (dW) for a specific neuron, based on its input, error, and the learning rate of the weight bias. Linearized measurement equation is expressed as follows:

$$\hat{U}_i = f(m, X_i) + \frac{\partial f}{\partial m}\Delta m \quad (49)$$

$$V_i = g(m, X_i) + \frac{\partial g}{\partial m}\Delta m \quad (50)$$

The quadratic cost function in Δm is:

$$\Delta m = \sum_i \sigma_i^{-2}(\hat{U}_i - U_i + \frac{\partial f}{\partial m}\Delta m)^2 + \cdots \quad (51)$$

Layer 3 Output Layer

The output layer is mathematically represented as:

$$U = \frac{1}{1+\exp^{-2X_i}}\left(W_{ij}^{HO} * H_i + B^o\right) \quad \text{for i, j} = 1,2,3 \ldots \quad (52)$$

where B^o is the bias of the output layer. After collecting data from individual DG units, the neural network is trained to adapt to the environment. The training process is repeated until validation is achieved. The performance of the training procedure is depicted in Figure 5, 6. As shown in Figure 5, the mean square error progressively decreases with each epoch, reaching its minimum value of 0.000064111 after 361 iterations. Once the network has completed learning from the training data, it is ready to map the input and output values. Figure 6 illustrates the regression plot, and the correlation coefficient (R) confirms that the FFNN was successfully trained using the provided data. The validation tests and overall network performance were satisfactory. Following successful training, the trained FFNN controller is implemented in MATLAB Simulink, and its performance is evaluated within a realistic islanded microgrid system. The overall working sequence is presented in Figure 7.

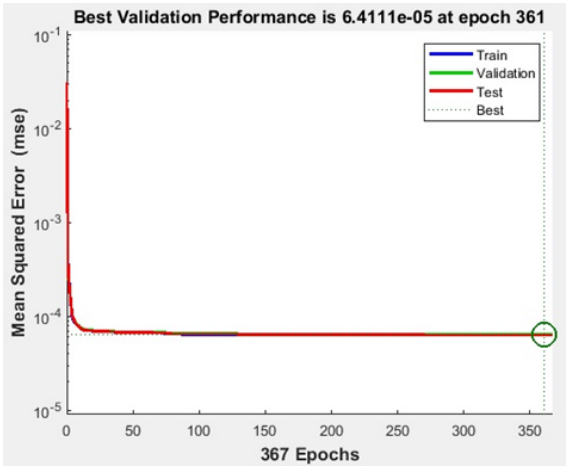

Figure 5. Validation Performance plot of SHLFFNN.

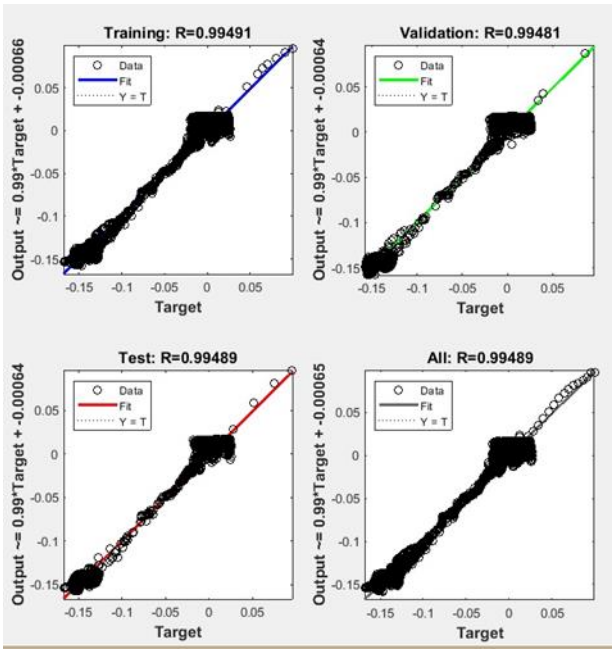

Figure 6. Training Regression plot of SHLFFNN.

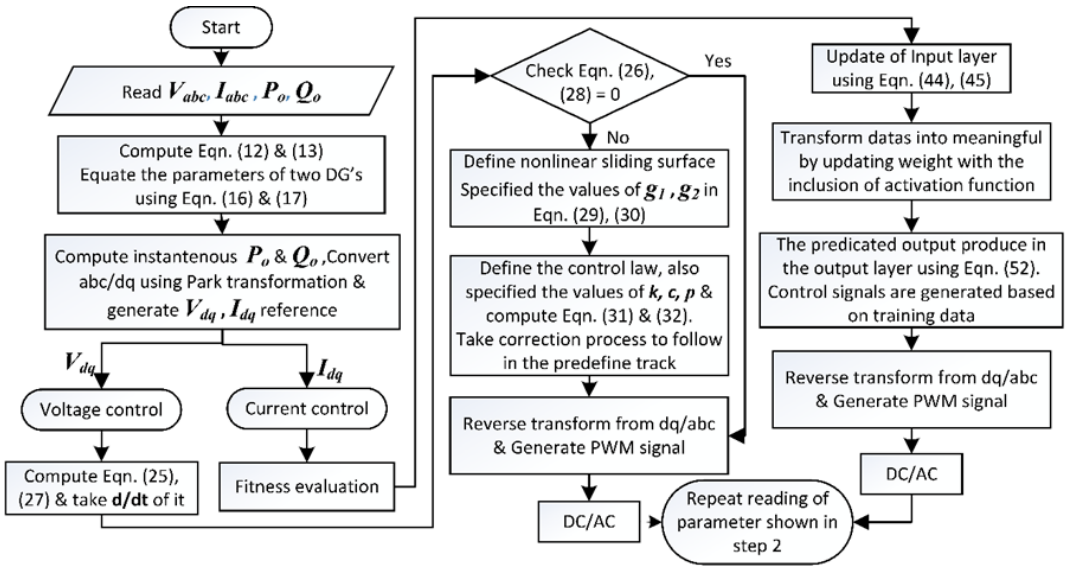

Figure 7. Overall working process of the controllers.

6. EVALUATION RESULTS

The proposed islanded microgrid system, shown in Fig. 1, is tested using MATLAB/Simulink. To ensure efficient execution, MATLAB/Simulink is configured in a discrete-time environment with a sample time of 5e-5. The graph is extracted from the scope after setting the execution time to one second. The parameters used in the simulation are chosen to be close to realistic values, as shown in Table 1, 2. The gain values and other control parameters for the proposed microgrid are carefully selected to suppress transients. Supervisory control is enabled with a period of 0.1s. The suggested control methods are tested to evaluate power-sharing performance under three different loading conditions, as well as voltage and frequency regulation. The obtained results are compared with the droop control method using PI anti-windup. The results are summarized below:

Case 1: Initially, a balanced load of P = 450 kW and Q = 180 kVar is connected. At 0.5 seconds, a balanced load starts to gradually increase, with P rising from 0 kW to 400 kW and Q increasing from 0 kVar to 70 kVar. This additional load is shared equally by both DGs.

Case 1 Results:

- **DG1 Output Voltage (Figure 8(a)):**

At the common terminal junction, the output voltage of DG1 is initially observed. With droop control combined with PI anti-windup, the voltage drops to 250V, far from the reference voltage of 480V. During the time interval 0 to 0.1 seconds, the slew rate is 585.439 V/ms (indicated in blue in Figure 8(a)). However, the voltage fails to reach the reference level between 0.1 to 0.2 seconds. In contrast, with the proposed controller, the output voltage at 0.1 seconds is improved to 350V (a 100V improvement), and the slew rate drops to 19.785 V/ms. During the 0.1 to 0.2-second interval, the proposed controller performs significantly better than the droop control with PI anti-windup. When an additional varying load is applied between 0.65 and 1 second, the existing controller causes the voltage to drop to 438V, failing to sustain the reference voltage. On the other hand, the proposed controller maintains a voltage of 460V (22V higher than the existing controller), and the voltage level remains more stable over the time period from 0 to 1 second.

- **DG2 Output Voltage (Figure 8(b)):**

The output voltage at DG2's common terminal junction is shown in Figure 8(b). With the existing controller, the output voltage fluctuates during the constant load period. Between 0 and 0.1 seconds, the proposed controller causes an initial voltage oscillation, but stability is eventually achieved. At 0.5 seconds, when the varying additional load is applied, the existing controller leads to significant voltage variation, and by 0.9 seconds, the voltage falls below 400V. In contrast, the proposed controller keeps the voltage above 430V. While both controllers experience a reduction in voltage due to the added load, the proposed controller ensures smoother voltage supply compared to the existing PI anti-windup controller.

Figure 9 shows the output frequency share between the two DGs using droop control with PI anti-windup. Under constant loading patterns, the output frequencies of both DGs exhibit different magnitudes.

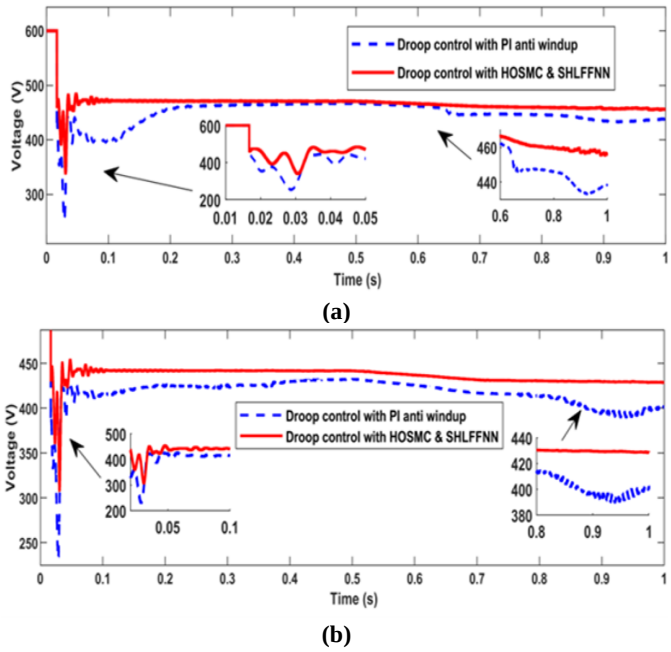

Figure 8. (a) Output voltage magnitude at the common terminal junction of DG1. **(b)** Output voltage magnitude at the common terminal junction of DG2.

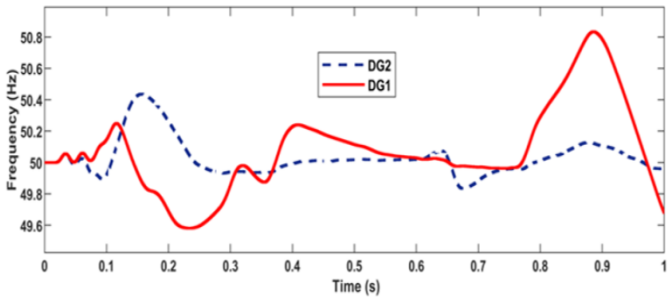

Figure 9. Output frequency shares of both DGs using droop control with PI anti-windup.

From t = 0.1 to 0.3 seconds, the output frequency of DG1 decreases, while DG2's frequency increases. When the varying additional load is applied, a noticeable difference in frequency magnitudes is observed between DG1 and DG2. Specifically, DG1's output frequency rises to 50.8Hz, whereas DG2's frequency remains relatively stable. This behavior highlights a lack of frequency synchronization between the two DGs.

The following characteristics are noted from the frequency response of both DGs:

- Rise time: 29.390 ms
- Slew rate: 11.287 V/s
- Undershoot: 1.967%.

Figure 10 illustrates the output frequency share between two DGs using droop control with HOSMC & SHLFFNN. During the constant load period, the output frequencies of both DGs rise equally. They then decrease toward the nominal value without any fluctuation, effectively following the reference trajectory. At t = 0.5 seconds, when a varying extra load is applied, the output frequency exhibits oscillations due to the load changes. Despite these variations, both DG1 and DG2 maintain the same frequency magnitude, demonstrating that the controllers in both DGs are capable of synchronizing and sharing the load equally.

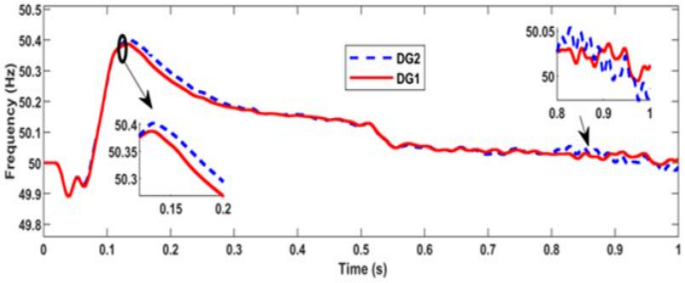

Figure 10. Output frequency shares of both DGs using droop control with HOSMC & SHLFFNN.

The frequency characteristics for both DGs are similar and are as follows:

- Rise time: 9.840 ms
- Slew rate: 9.548 V/s
- Undershoot: 1.602%.

Figures 11 (a) and (b) illustrate the real and reactive power sharing between the two DGs using droop control with the PI anti-windup controller. During the constant load period, the real and reactive power sharing oscillates between the DGs, and there is unequal distribution of both real and reactive power. The power share of DG2 fluctuates significantly, with real power decreasing while reactive power increases.

At t = 0.5 seconds, when a varying extra load is introduced, the real power supplied by DG2 drops further, while its reactive power supply increases. In contrast, DG1 maintains stable power sharing, contributing more real power. This indicates that the PI anti-windup controller is ineffective in ensuring balanced real and reactive power sharing between the DGs.

Figures 12 (a) and (b) depict the real and reactive power sharing between two DGs using droop controllers with HOSMC and SHLFFNN controllers. During the constant load period, both DGs share real and reactive power equally, with only minimal variation initially. At t = 0.5 seconds, when varying extra load is added, both real and reactive power sharing gradually increases. The steady-state error is minimized and approaches zero, demonstrating that the proposed controller effectively handles the real and reactive power demands between the DGs.

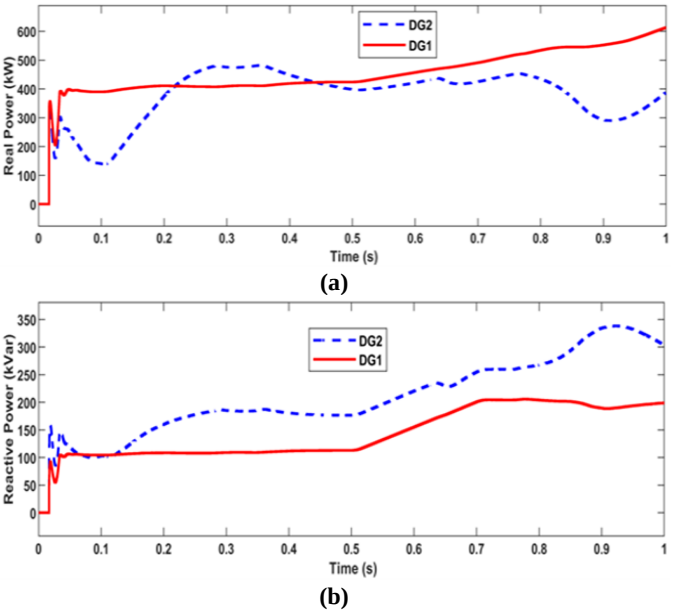

Figure 11. (a) Real power share between two DGs using droop control with PI anti-windup. **(b)** Reactive power share between two DGs using droop control with PI anti-windup.

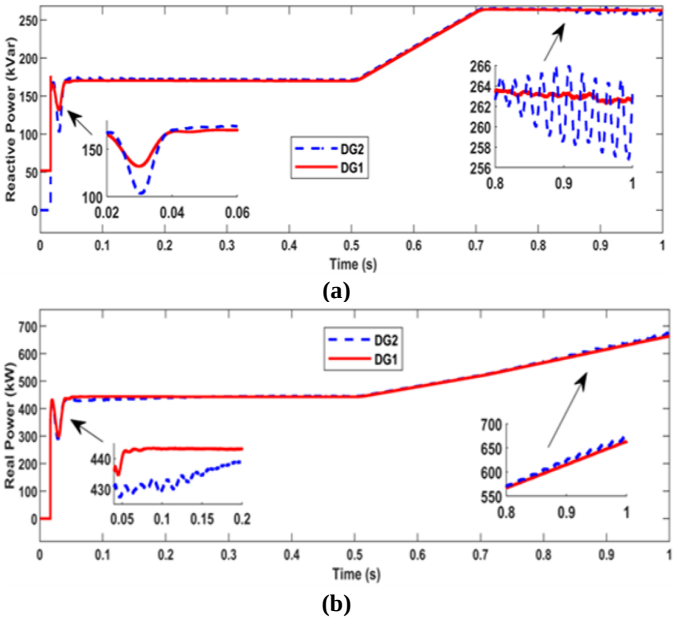

Figure 12. (a) Reactive power share between two DGs using droop control with HOSMC and SHLFFNN. **(b)** Real power share between two DGs using droop control with HOSMC and SHLFFNN.

Case 2: The unbalanced load scenario, shown in Figure 13 (a) and (b), includes a resistive balanced load of P = 50 KW throughout the operation. At t = 0.5 seconds, a gradually increasing load is introduced, with real power rising from P = 0 KW to P = 400 KW and reactive power increasing from Q = 0 KVar to Q = 100 KVar, distributed between both DGs.

The output voltage magnitude of DG1 is shown in Figure 14(a). From t = 0 to 0.2 seconds, the output voltage of the existing controller fluctuates, dropping below 200V, while the reference is 480V. The slew rate is 908.489 V/ms, as indicated in blue in Fig. 14(a). During this period, the proposed controller performs better. The output voltage stabilizes at 380V, and the slew rate improves to 451.048 V/ms. At t = 0.5 seconds, when the unbalanced load reaches its maximum, a gradually increasing load is added. The existing controller's output voltage begins to decrease, and at t = 0.8 seconds, it reaches 470V. However, the output voltage level fails to sustain the reference voltage. In contrast, the proposed controller's output voltage drops to 478V at t = 0.6 seconds, representing an 8V improvement. The overall output voltage response remains steady, consistently supplying the reference voltage.

Figure 14(b) illustrates the output voltage magnitude at DG2. Initially, the output voltage of the existing controller oscillates more than that of the proposed controller. At t = 0.5 seconds, when the unbalanced load reaches its maximum, a gradually increasing load is added. The existing controller's output voltage decreases to 465V, failing to maintain the standard voltage level. On the other hand, the proposed controller's output voltage drops to 475V, which is a 5V reduction from the reference. The proposed controller's output voltage is more stable and resistant to load changes, ensuring a more consistent supply. The output frequency share using droop control with PI anti-windup is shown in Fig. 15. From t = 0 to 0.25 seconds, the output frequency of both DGs increases. At 0.25 seconds, DG1's output frequency starts to decrease, approaching 50Hz.

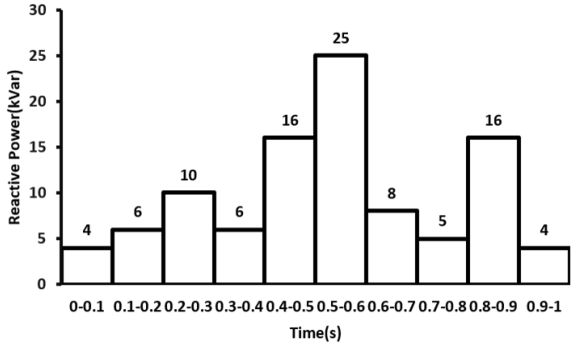

(a)

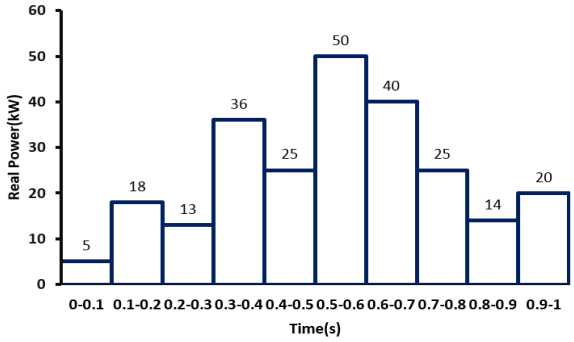

(b)

Figure 13. (a) Reactive power loading pattern (b) Real power loading pattern.

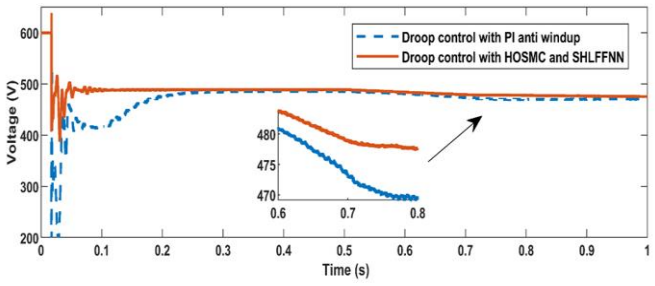

(a)

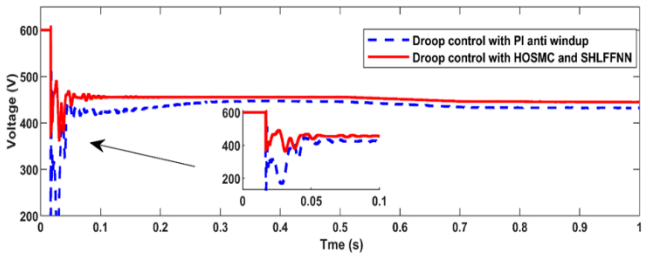

(b)

Figure 14. (a) Output voltage magnitude at the common terminal junction of DG1. **(b)** Output voltage magnitude at the common terminal junction of DG2.

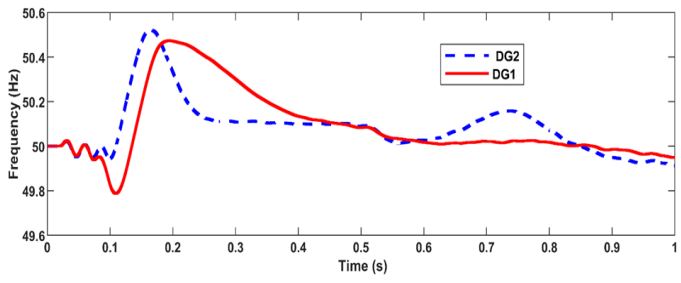

Figure 15. Output frequency shares of both DGs using droop control with PI anti-windup.

Meanwhile, at t = 0.4 seconds, the output frequency of DG2 reaches the standard frequency. At 0.5 seconds, when the unbalanced load reaches its maximum, a gradually increasing load is added. DG2's frequency oscillates and fails to sustain the reference level. In contrast, DG1's frequency response remains unaffected by the load changes. The unequal frequency response between the two DGs, especially during load changes, could potentially impact the life span of the equipment.

The following characteristics are observed from the frequency response of both DGs:

- DG1: Rise time = 33.848 ms, Slew rate = 10.691 V/s, Undershoot = 1.988%.
- DG2: Rise time = 29.718 ms, Slew rate = 10.985 V/s, Undershoot = 1.986%.

The output frequency of the DGs using droop control with HOSMC & SHLFFNN is shown in Figure 16. At 0.15 seconds, the frequency response of both DGs increases and reaches a maximum frequency of 50.4 Hz. By 0.52 seconds, the frequency response decreases and stabilizes at 50 Hz. At 0.5 seconds, when the unbalanced load reaches its maximum magnitude, a gradually increasing load is added. The frequencies of both DGs are shared equally, with only a slight deviation, which remains within the standard limit. This indicates that the controller is capable of synchronizing and ensuring equal load sharing between the DGs. The frequency characteristics are mostly similar for both DGs:

- DG1: Rise time = 8.095 ms, Slew rate = 11.623 V/s, Undershoot = 1.944%.
- DG2: Rise time = 7.924 ms, Slew rate = 12.052 V/s, Undershoot = 1.757%.

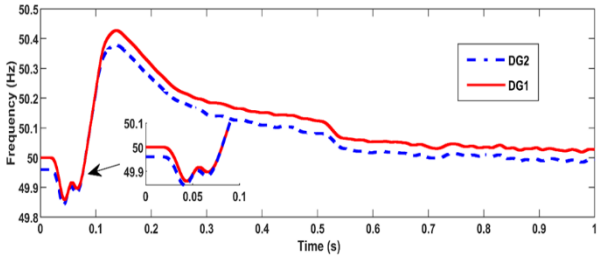

Figure 16. Output frequency shares of both DGs using droop control with HOSMC & SHLFFNN.

The real and reactive power sharing between the two DGs using droop controllers with PI anti-windup controllers is shown in Figure 17 (a) and (b). The power sharing between the DGs fluctuates, with DG1 maintaining stable real and reactive power sharing, while DG2's power sharing is unstable. Initially, the real and reactive power sharing of DG2 fluctuates more than that of DG1. As the load increases, the real power share of DG2 decreases. At 0.5 seconds, when the extra load is added and the unbalanced load reaches its maximum value, the real power share of DG2 drops significantly. During this time, the real power of DG1 and the reactive power of both DGs attempt to meet the load demand. However, the real power share of DG2 fails to maintain a stable supply. From Figures 17 (a) and (b), it is evident that there is unequal sharing of real and reactive power between the DGs. This behavior demonstrates that the PI anti-windup controller is ineffective in ensuring equal real and reactive power sharing among the DGs. The real and reactive power sharing between the two DGs using droop controllers with HOSMC & SHLFFNN controllers is illustrated in Figure 18 (a) and (b). During the initial period, both real and reactive power sharing fluctuate but later stabilize. As the load begins to increase, the power-sharing between the DGs remains

unaffected. An equal magnitude of reactive power is shared between the DGs, while the real power sharing is unequal, though stable. At 0.5 seconds, when the unbalanced load reaches its maximum magnitude and the gradually increasing load is added, both DGs supply the required real and reactive power as per the demand. As the unbalanced load decreases and the extra load increases, the real and reactive power supply from the DGs remains stable. The steady-state error is minimized and approaches zero. This proves that the proposed controller effectively manages the real and reactive power sharing between the DGs, meeting their actual power demands.

Case 3: Initially, a balanced load of P = 350 kW and Q = 200 kVar is connected. At 0.5 seconds, a gradually increasing balanced load (P = 0 kW to 400 kW, Q = 0 kVar to 80 kVar) is added to both DGs. Additionally, an asynchronous motor with a rating of 3.6 kW is connected as an extra load throughout the operation, with the loading pattern shown in Figure 19.

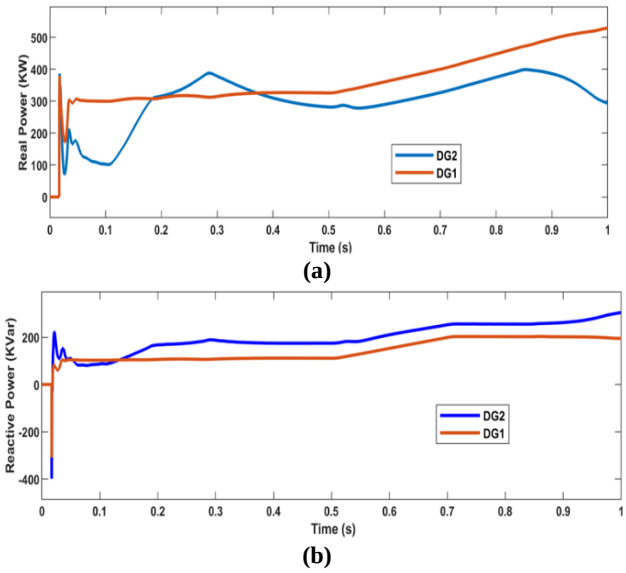

Figure 17. (a) Real power share between two DGs using droop control with PI anti-windup. **(b)** Reactive power share between two DGs using droop control with PI anti-windup.

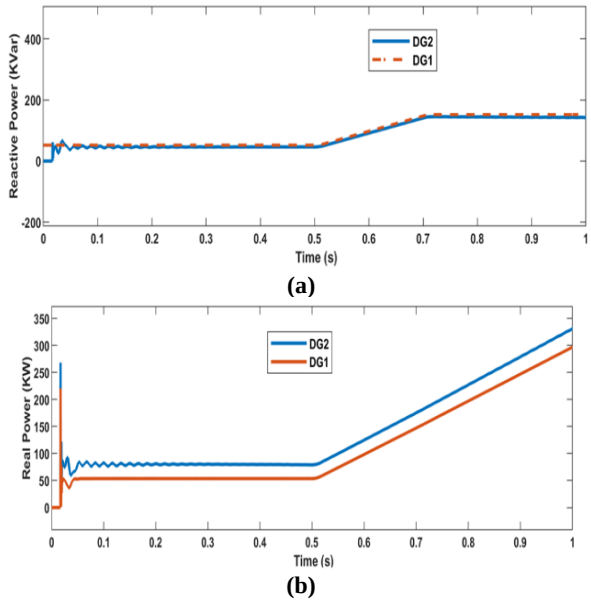

Figure 18. (a) Reactive power share between two DGs using droop control with HOSMC & SHLFFNN. **(b)** Real power share between two DGs using droop control with HOSMC & SHLFFNN.

The real and reactive power sharing between the two DGs using droop control with PI anti-windup is shown in Figure 20 (a) and (b). The real and reactive power share of DG1 remains stable, while the power sharing of DG2 is unstable. Throughout the operation, a torque-varying asynchronous motor load is added. Initially, at t = 0.4 sec, there is no equal power sharing between the DGs. At t = 0.5 sec, as the gradually increasing load is added, the real power sharing of DG2 decreases, while DG1's real power sharing increases as the load rises. During this process, the reactive power share of both DGs increases, with DG2's share being larger than DG1's. The overall power-sharing performance is influenced by the torque variations of the asynchronous motor. This indicates that the PI anti-windup controller is less resilient to load variations, proving that it is inefficient in managing real and reactive power sharing between the DGs. The real and reactive power sharing between the DGs using droop control with HOSMC & SHLFFNN is shown in Figure 21 (a) and (b). Between t = 0 and t = 0.1 sec, the real and reactive power sharing oscillates. However, the real and reactive power sharing among the DGs remains nearly equal in magnitude. The addition of a torque-varying asynchronous motor load throughout the operation does not cause any disturbances in the real and reactive power sharing. At 0.5 sec, when a gradually increasing load is added, both DGs supply the corresponding real and reactive power demand equally. This demonstrates that the proposed controller is resilient to disturbances and load variations, maintaining stable power sharing.

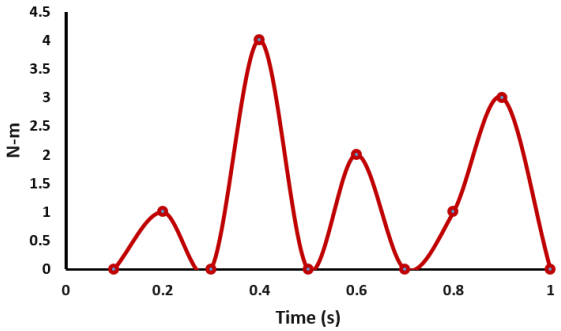

Figure 19. Torque pattern input to the asynchronous motor.

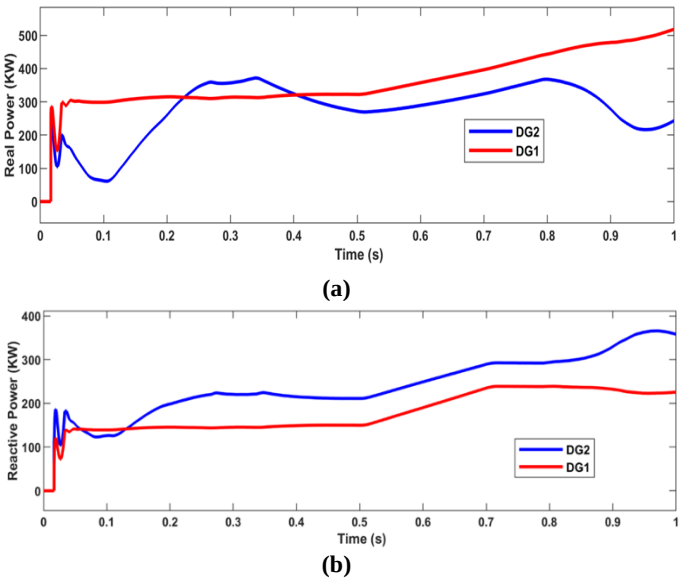

Figure 20. (a) Real power share between two DGs using droop control with PI anti-windup. **(b)** Reactive power share between two DGs using droop control with PI anti-windup.

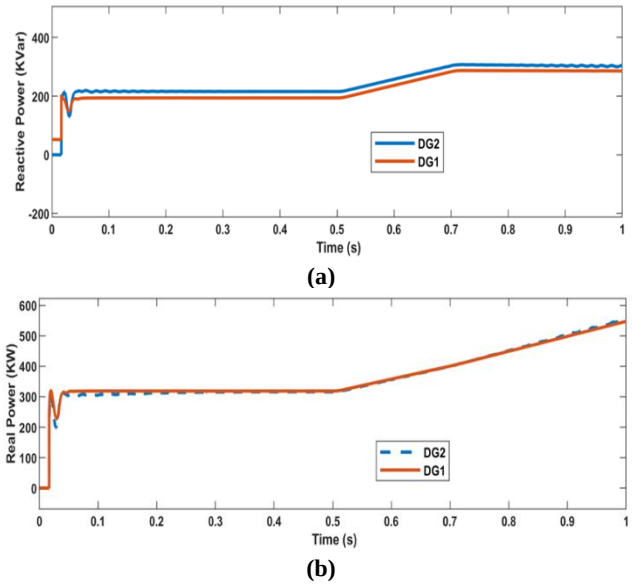

Figure 21. (a) Reactive power share between two DGs using droop control with HOSMC & SHLFFNN. **(b)** Real power share between two DGs using droop control with HOSMC & SHLFFNN.

The percentage voltage and frequency regulation are calculated using the following equation, as Eq. (53), (54):

$$\%VR = \frac{V_{nl}-V_{fl}}{V_{fl}} \times 100 \quad (53)$$

$$\%fR = \frac{f_r-f_{fl}}{f_{fl}} \times 100 \quad (54)$$

To confirm the viability of the suggested control procedures, the output voltage and frequency regulation performances of the proposed controller, SMC, and droop control with PI anti-windup are compared using the formulas defined in Eq. (53) and (54). The comparisons, shown in Figure 22, 23, respectively, are performed under unbalanced load conditions as described in Case 2.

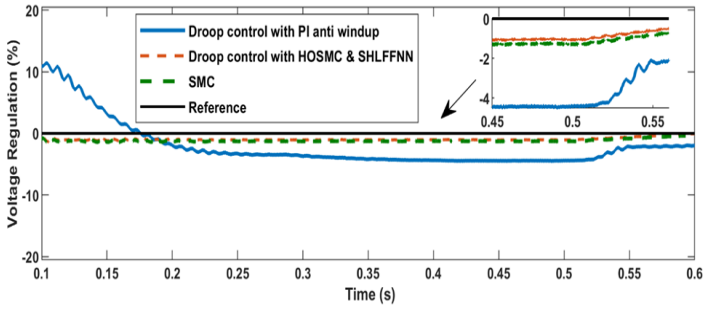

Figure 22. Output voltage regulation comparison of the proposed controller, Sliding Mode Control (SMC), and droop control with PI anti-windup.

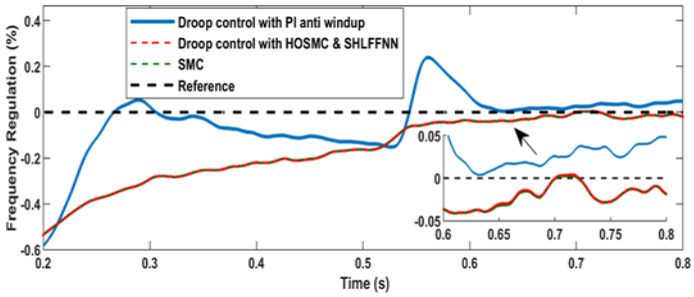

Figure 23. Output frequency regulation comparison of the proposed controller, Sliding Mode Control (SMC), and droop control with PI anti-windup.

The output voltage and frequency regulation results are directly related to the real and reactive power changes in the DGs. Therefore, the performance verification conducted in voltage and frequency regulation is valid.

At t = 0.2 sec and t = 0.5 sec, the voltage regulation percentages for the proposed controller are -1.05 and -0.13, respectively, which are closer to the reference value. In contrast, the voltage regulation percentages for SMC are -1.28 and -0.35, respectively. Additionally, the voltage regulation percentages for droop control with PI anti-windup are -7.61 and -6.93, respectively. A higher percentage indicates a greater deviation from the reference. The characteristics comparison of voltage regulation is shown in Table 3.

Table 3. Voltage regulation characteristics comparison between the controllers.

Performance Indicator	Proposed droop control with HOSMC and SHLFFNN	SMC	Droop control with PI anti-windup
Percentage overshoot	51.81	51.99	1052.27
Rise time (μs)	109.563	109.56	178.55
Fall time(μs)	142.70	142.70	732.79

The frequency regulation deviates initially in all the controllers but improves afterward. At t = 0.7 sec, the frequency regulation for the proposed controller is -0.01, which is closer to the reference value than SMC (-0.02) and droop control with PI anti-windup (-0.28). The frequency regulation of the proposed controller remains stable despite load changes. The voltage and frequency comparisons with the other existing and proposed controllers are given in Table 4. Table 5 shows the controllers' responses to voltage and frequency control operations in the islanded microgrid. These results conclude that the proposed controller is more capable of supplying the required real and reactive power than the other two controllers mentioned.

Table 4. Voltage and frequency comparison between the existing and proposed controllers

Controller	Voltage (V) (Ref. = 480V)							
	Case I				Case II			
	DG1		DG2		DG1		DG2	
	t=0.1s		t=0.65-1s	t=0.9s	t=0-0.2s	t=0.8s	t=0.5s	
Droop control with PI anti-windup	250		438	400	280	470	465	
Proposed droop control with HOSMC and SHLFFNN	350		460	430	380	478	475	
Controller	**Frequency (Hz) (Ref. = 50Hz)**							
	Case I				Case II			
	DG1		DG2		DG1		DG2	
	Min	Max	Min	Max	Min	Max	Min	Max
Droop control with PI anti-windup	49.6	50.8	49.8	50.4	49.6	50.4	49.89	50.5
Proposed droop control with HOSMC and SHLFFNN	49.9	50.4	49.9	50.4	49.85	50.4	49.84	50.38

Table 5. Reaction of different controllers to voltage and frequency control operation in an islanded microgrid.

Controller	Voltage	Frequency
(P-f/Q-V) + filter and (P-f/Q-V) + derivative (Rokrok et al., 2018)	Poor voltage regulation	Inability to handle non-linear loads as a result frequency is unstable
PI and Adaptive droop control (Roudbari et al., 2020)	Voltage drops during the load increases	Frequency reduced during the load increases
Model Predictive Control (Joshal & Gupta, 2023)	Introduce complexities and increased computational requirements. So, it required support from the other advanced controllers for steady voltage.	Introduce time delay and affected data reliability. So, the frequency regulation required a high-speed operated controller.
Fuzzy Logic Controller (Roudbari et al., 2020)	Minimal change in frequency during load increase up to 10kW and 10 KVar	Load handling capacity is low Achieve stable voltage when 10kW and 10kVar loads are added.
Proposed droop control with HOSMC and SHLFFNN	Minimal change in frequency during load increase up to 400kW and 100 KVar	Capable of handling large loads with little variation when loads of 400kW and 100kVar are added.

7. CONCLUSIONS

Simulations and studies were conducted to investigate how the isolated microgrid operates under three different loading patterns. A new strategy based on droop control with HOSMC and SHLFFNN is proposed to address the power-sharing issues found in droop controllers with the PI anti-windup control method. The controller's performance is tested and validated by applying it to the proposed DG microgrid system and comparing it to different controllers. The proposed controller effectively resolves the drawbacks of droop controllers with PI anti-windup control, as demonstrated by the results. It accurately shares real and reactive power between the DG units and minimizes damping oscillations caused by significant load fluctuations and uncertainties. The results show that the suggested droop control with HOSMC and SHLFFNN provides better steady-state operation, with smaller percentages of overshoot, rise time, and fall time compared to existing approaches. Moreover, it effectively controls the microgrids voltage and frequency as the load varies. Therefore, the performance of the proposed droop control with HOSMC and SHLFFNN is determined to be superior to that of both the droop control with PI anti-windup and the SMC controller. However, the proposed controller is currently limited to regulating voltage and frequency within constant load and load variation limits. Future work will focus on upgrading the controller to handle higher load capacities.

8. ACKNOWLEDGEMENT

We are thankful to the Department of Electrical Engineering at both Manipur Technical University and the National Institute of Technology for providing us access to their laboratories.

REFERENCES

1. Abjadi, N. R. (2024). Nonsingular Terminal Sliding Mode Control for Islanded Inverter-Based Microgrids. *Journal of Operation and Automation in Power Engineering*, *12*(1). https://doi.org/10.22098/joape.2023.10543.1750

2. Abrishamifar, A., Ahmad, A. A., & Mohamadian, M. (2012). Fixed switching frequency sliding mode control for single-phase unipolar inverters. *IEEE Transactions on Power Electronics*, *27*(5). https://doi.org/10.1109/TPEL.2011.2175249

3. Al-Saedi, W., Lachowicz, S., Habibi, D., & Bass, O. (2012). Power quality enhancement in autonomous microgrid operation using particle swarm optimization. *Int. J. Elect. Power Energy Syst., 42(1), 139-149.* https://doi.org/10.1109/ISGT-Asia.2011.6257101

4. Amarendra, K., Teeparthi, K., Vamsi, Y. R., Veeramsetty, V., & Thota, V. V. N. P. (2023). Load Frequency Control of an Interconnected Microgrid Using MGO-based 2DOF-PID Controller. *2023 7th International Conference on Computer Applications in Electrical Engineering-Recent Advances: Sustainable Transportation Systems, CERA 2023*. https://doi.org/10.1109/CERA59325.2023.10455360

5. Anbazhagan, S., & Kumarappan, N. (2011). Day-ahead price forecasting in asia's first liberalized electricity market using artificial neural networks. *International Journal of Computational Intelligence Systems*, *4*(4). https://doi.org/10.1080/18756891.2011.9727806

6. Cucuzzella, M., Incremona, G. P., & Ferrara, A. (2015). Master-slave second order sliding mode control for microgrids. *Proceedings of the American Control Conference*, *2015-July*. https://doi.org/10.1109/ACC.2015.7172149

7. Cucuzzella, M., Incremona, G. P., & Ferrara, A. (2015a). Design of Robust Higher Order Sliding Mode Control for Microgrids. *IEEE Journal on Emerging and Selected Topics in Circuits and Systems*, *5*(3). https://doi.org/10.1109/JETCAS.2015.2450411

8. Cucuzzella, M., Incremona, G. P., & Ferrara, A. (2015b). Third order sliding mode voltage control in microgrids. *2015 European Control Conference, ECC 2015*. https://doi.org/10.1109/ECC.2015.7330895

9. Damiano, A., Musio, C., & Marongiu, I. (2015). Experimental validation of a dynamic energy model of a battery electric vehicle. *2015 International Conference on Renewable Energy Research and Applications, ICRERA 2015*. https://doi.org/10.1109/ICRERA.2015.7418523

10. Das, D. C., Roy, A. K., & Sinha, N. (2012). GA based frequency controller for solar thermal-diesel-wind hybrid energy generation/energy storage system. *International Journal of Electrical Power and Energy Systems*, *43*(1). https://doi.org/10.1016/j.ijepes.2012.05.025

11. El-Fergany, A. A., & El-Hameed, M. A. (2017). Efficient frequency controllers for autonomous two-area hybrid microgrid system using social-spider optimiser. *IET Generation, Transmission and Distribution*, *11*(3). https://doi.org/10.1049/iet-gtd.2016.0455

12. Gamez Urias, M. E., Sanchez, E. N., & Ricalde, L. J. (2015). Electrical Microgrid Optimization via a New Recurrent Neural Network. *IEEE Systems Journal*, *9*(3). https://doi.org/10.1109/JSYST.2014.2305494

13. Geravandi, M., & Moradi CheshmehBeigi, H. (2022). The Problem of Resilient Stochastic Unit Commitment with Consideration of Existing Uncertainties Using the Rate of Change of Frequency. *Journal of Renewable Energy and Environment*, *9*(4). https://doi.org/10.30501/jree.2022.306473.1262

14. Guerrero, J. M., Vasquez, J. C., Matas, J., De Vicuña, L. G., & Castilla, M. (2011). Hierarchical control of droop-controlled AC and DC microgrids - A general approach toward standardization. *IEEE Transactions on Industrial Electronics*, *58*(1). https://doi.org/10.1109/TIE.2010.2066534

15. Habibi, S. I., Sheikhi, M. A., Khalili, T., Abadi, S. A. G. K., Bidram, A., & Guerrero, J. M. (2024). Multiagent-Based Nonlinear Generalized Minimum Variance Control for Islanded AC Microgrids. *IEEE Transactions on Power Systems*, *39*(1). https://doi.org/10.1109/TPWRS.2023.3239793

16. Hassan Moradi CheshmehBeigi, M. G. (2023). Unit Commitment Risk Evaluation Considering Load Uncertainty and Wind Power. *Journal of Energy Management and Technology*, *7*(3), 134–141. https://dx.doi.org/10.22109/JEMT.2023.311870.1342

17. Hassan, M. A., & Abido, M. A. (2011). Optimal design of microgrids in autonomous and grid-connected modes using particle swarm optimization. *IEEE Transactions on Power Electronics*, *26*(3). https://doi.org/10.1109/TPEL.2010.2100101

18. Hoa Thi Pham, X. (2020). Power sharing strategy in islanded microgrids using improved droop control. *Electric Power Systems Research*, *180*. https://doi.org/10.1016/j.epsr.2019.106164

19. Hong, C. M., & Chen, C. H. (2014). Intelligent control of a grid-connected wind-photovoltaic hybrid power systems. *International Journal of Electrical Power and Energy Systems*, *55*. https://doi.org/10.1016/j.ijepes.2013.10.024

20. Hossain, M. A., & Pota, H. R. (2015). Voltage tracking of a single-phase inverter in an islanded microgrid. *International Journal of Renewable Energy Research*, *5*(3). https://doi.org/10.20508/ijrer.v5i3.2415.g6643

21. Jalilian, M., Rastgou, A., Kharrati, S., & Hosseini-Hemati, S. (2023). Frequency Stability of Hybrid Power System in the Presence of Superconducting Magnetic Energy Storage and Uncertainties. *Journal of Operation and Automation in Power Engineering*, *11*(4). https://doi.org/10.22098/joape.2023.9829.1686

22. Joshal, K. S., & Gupta, N. (2023). Microgrids with Model Predictive Control: A Critical Review. In *Energies* (Vol. 16, Issue 13). https://doi.org/10.3390/en16134851

23. Jumani, T. A., Mustafa, M. W., Alghamdi, A. S., Rasid, M. M., Alamgir, A., & Awan, A. B. (2020). Swarm Intelligence-Based Optimization Techniques for Dynamic Response and Power Quality Enhancement of AC Microgrids: A Comprehensive Review. *IEEE Access*, *8*. https://doi.org/10.1109/ACCESS.2020.2989133

24. Keyvani, B., Fani, B., Karimi, H., Moazzami, M., & Shahgholian, G. (2022). Improved Droop Control Method for Reactive Power Sharing in Autonomous Microgrids. *Journal of Renewable Energy and Environment*, *9*(3). https://doi.org/10.30501/jree.2021.298138.1235

25. Ko, J. S., Huh, J. H., & Kim, J. C. (2020). Overview of maximum power point tracking methods for PV system in micro grid. In *Electronics (Switzerland)* (Vol. 9, Issue 5). https://doi.org/10.3390/electronics9050816

26. Ma, J., Wang, X., & Lan, X. (2012). Small-signal stability analysis of microgrid based on perturbation theory. *Asia-Pacific Power and Energy Engineering Conference, APPEEC*. https://doi.org/10.1109/APPEEC.2012.6306946

27. Makarenkov, O. (2017). A simple proof of the Lyapunov finite-time stability theorem. *Comptes Rendus. Mathématique*, *355*(3). https://doi.org/10.1016/j.crma.2017.02.003

28. Mamta, Singh, V. P., Waghmare, A. V., Meena, V. P., Benedetto, F., & Varshney, T. (2024). Rank Exponent Method Based Optimal Control of AGC for Two-Area Interconnected Power Systems. *IEEE Access*, *12*. https://doi.org/10.1109/ACCESS.2024.3373043

29. Mawuntu, N. N., Mu, B. Q., Doukhi, O., & Lee, D. J. (2023). Modeling of the Battery Pack and Battery Management System towards an Integrated Electric Vehicle Application. *Energies*, *16*(20). https://doi.org/10.3390/en16207165

30. Mishra, S. (2013). Permanent magnet synchronous generator based stand-alone wind energy supply system. *IEEE Power & Energy Society General Meeting* (pp. 1-1). Vancouver, BC, Canada. https://doi.org/10.1109/pesmg.2013.6673039

31. Moazzami, M., Gharehpetian, G. B., Shahinzadeh, H., & Hosseinian, S. H. (2017). Optimal locating and sizing of DG and D-STATCOM using Modified Shuffled Frog Leaping Algorithm. *2nd Conference on Swarm Intelligence and Evolutionary Computation, CSIEC 2017 - Proceedings*. https://doi.org/10.1109/CSIEC.2017.7940157

32. Micallef, A., Apap, M., Spiteri-Staines, C., Guerrero, J. M., & Vasquez, J. C. (2014). Reactive power sharing and voltage harmonic distortion compensation of droop controlled single phase islanded microgrids. *IEEE Transactions on Smart Grid*, *5*(3). https://doi.org/10.1109/TSG.2013.2291912

33. Pandey, S. K., Mohanty, S. R., Kishor, N., & Catalão, J. P. S. (2014). Frequency regulation in hybrid power systems using particle swarm optimization and linear matrix inequalities based robust controller design. *International Journal of Electrical Power and Energy Systems*, *63*. https://doi.org/10.1016/j.ijepes.2014.06.062

34. Poonahela, I., Krama, A., Bayhan, S., Fesli, U., Shadmand, M. B., Abu-Rub, H., & Begovic, M. M. (2023). Hierarchical Model-Predictive Droop Control for Voltage and Frequency Restoration in AC Microgrids. *IEEE Open Journal of the Industrial Electronics Society*, *4*. https://doi.org/10.1109/OJIES.2023.3240070

35. Rangu, S. K., Lolla, P. R., Dhenuvakonda, K. R., & Singh, A. R. (2020). Recent trends in power management strategies for optimal operation of distributed energy resources in microgrids: A comprehensive review. In *International Journal of Energy Research* (Vol. 44, Issue 13). https://doi.org/10.1002/er.5649

36. Rokrok, E., Shafie-khah, M., & Catalão, J. P. S. (2018). Review of primary voltage and frequency control methods for inverter-based islanded microgrids with distributed generation. In *Renewable and Sustainable Energy Reviews* (Vol. 82). https://doi.org/10.1016/j.rser.2017.10.022

37. Roudbari, E. S., Beheshti, M. T. H., & Rakhtala, S. M. (2020). Voltage and frequency regulation in an islanded microgrid with PEM fuel cell based on a fuzzy logic voltage control and adaptive droop control. *IET Power Electronics*, *13*(1). https://doi.org/10.1049/iet-pel.2019.0592

38. Šabanovic, A. (2011). Variable structure systems with sliding modes in motion control - A survey. *IEEE Transactions on Industrial Informatics*, *7*(2). https://doi.org/10.1109/TII.2011.2123907

39. Sarkar, S. K., & Das, S. K. (2018). High performance nonlinear controller design for AC and DC machines: partial feedback linearization approach. *International Journal of Dynamics and Control*, *6*(2). https://doi.org/10.1007/s40435-017-0330-x

40. Shayeghi, H., & Rahnama, A. (2024). Frequency Regulation of a Standalone Interconnected AC Microgrid Using Innovative Multistage TDF(1+FOPI) Controller. *Journal of Operation and Automation in Power Engineering*, *12*(2), 121–133. https://doi.org/10.22098/joape.2023.10668.1768

41. Sofla, M. A., & Gharehpetian, G. B. (2011). Dynamic performance enhancement of microgrids by advanced sliding mode controller. *International Journal of Electrical Power and Energy Systems*, *33*(1). https://doi.org/10.1016/j.ijepes.2010.08.011

42. Tran, Q. T. T., Di Silvestre, M. L., Sanseverino, E. R., Zizzo, G., & Pham, T. N. (2018). Driven primary regulation for minimum power losses operation in islanded microgrids. *Energies*, *11*(11). https://doi.org/10.3390/en11112890

43. Vigneysh, T., & Kumarappan, N. (2016). Artificial Neural Network Based Droop-Control Technique for Accurate Power Sharing in an Islanded Microgrid. *International Journal of Computational Intelligence Systems*, *9*(5). https://doi.org/10.1080/18756891.2016.1237183

44. Wu, L., Yang, H., Wei, J., & Jiang, W. (2024). Research on Distributed Coordination Control Method for Microgrid System Based on Finite-Time Event-Triggered Consensus Algorithm. *Chinese Journal of Electrical Engineering*, *10*(2), 103–115. https://doi.org/10.23919/CJEE.2024.000053